Metal–Ligand Exchange Coupling Promotes Iron-Catalyzed Electrochemical CO₂ Reduction at Low Overpotentials

Jeffrey S. Derrick[1], Matthias Loipersberger[1], Diana A. Iovan[1], Peter T. Smith[1], Khetpakorn Chakarawet[1], Jeffrey R. Long[1,2,3], Martin Head-Gordon[1,4], & Christopher J. Chang[1,4,5]*

Affiliations:

[1]Department of Chemistry, University of California, Berkeley, CA, 94720, USA.

[2]Department of Chemical and Biomolecular Engineering, University of California, Berkeley, CA, 94720, USA.

[3]Materials Sciences Division, Lawrence Berkeley National Laboratory, Berkeley, CA, 94720, USA.

[4]Chemical Sciences Division, Lawrence Berkeley National Laboratory, Berkeley, CA, 94720, USA.

[5]Department of Molecular and Cell Biology, University of California, Berkeley, CA, 94720, USA.

*Correspondence to: chrischang@berkeley.edu

ABSTRACT: Biological and heterogenous catalysts for electrochemical CO_2 reduction often exhibit a high degree of electronic delocalization that serves to minimize overpotential and maximize selectivity over hydrogen evolution. Here, we report a molecular iron(II) complex that achieves a similar feat as a result of strong metal–ligand exchange coupling. This interaction promotes an open-shell singlet electronic structure that drives the electrochemical reduction of CO_2 to CO with over 90% selectivity and turnover frequencies of $100,000 \text{ s}^{-1}$ at low overpotentials, with no degradation over 20 hours. The decrease in the thermodynamic barrier engendered by this strong metal–ligand exchange coupling enables homogeneous CO_2 reduction catalysis in water without compromising reaction selectivity.

INTRODUCTION

The electrochemical carbon dioxide reduction reaction provides opportunities to synthesize value-added products in a sustainable manner.[1,2] Efficient catalysts for this reaction are required to selectively drive CO_2 reduction over the thermodynamic and kinetically competitive hydrogen evolution reaction[3]. Biological[4], heterogenous[5], and molecular[3] catalysts have been studied for CO_2 reduction, and molecular systems in particular offer potential advantages such as their small size, relative to enzymes, and the fact that they can be tuned with a level of atomic precision that is inaccessible with heterogeneous materials. However, despite advances in the development of molecular catalysts with highly specialized ligand scaffolds, including cyclams[6,7], porphyrins and phthalocyanines[8–10], and tricarbonyl-bipyridines[11,12], it remains a challenge to design molecules that exhibit low overpotentials, high turnover numbers, and compatibility with aqueous electrolytes. In this regard, one key advantage of biological and heterogeneous catalysts is their ability to minimize overpotential and maximize selectivity for CO_2 reduction via electronic delocalization, either through electron-tunneling pathways or a high local density of states,

respectively. Such systems can thereby achieve organization and separation of reducing equivalents in a way that is challenging to design in molecular systems.

Previous work from our laboratories has explored the chemistry of the PY5Me$_2$ ligand (2,6-bis(1,1-bis(2-pyridyl)ethyl)pyridine) and its molybdenum[13–15] and cobalt[15,16] derivatives as catalysts for the hydrogen evolution reaction. We reasoned that by incorporating a redox-active pendant such as terpyridine within this ligand scaffold, it would be possible to increase metal–ligand orbital mixing and delocalization of electron density away from the metal center to favor CO$_2$ reduction (Figure 1a). Indeed, the suppression of metal-centered reduction can limit the formation of off-pathway intermediates necessary for hydrogen evolution (e.g., metal hydrides)[17,18] and thereby favor CO$_2$ reduction catalysis. Our synthetic approach was inspired by mononuclear iron hydrogenase enzymes, which catalyze the reduction of methenyl-H$_4$MPT$^+$ to methylene-H$_4$MPT in methanogenic archaea[19]. In these systems, heterolysis of H$_2$ and hydride shuttling is enabled by a single redox-innocent iron(II) site that synergistically interacts with a redox non-innocent guanyl pyridinol cofactor in the primary coordination sphere to provide reducing equivalents (Figure. 1a).

Here we report an iron polypyridine complex [Fe(tpyPY2Me)(CH$_3$CN)]$^{2+}$ (tpyPY2Me = 6-(1,1-di(pyridin-2-yl)ethyl)-2,2′:6′,2″-terpyridine), that is the first example of a molecule to demonstrate this principle of electronic delocalization. In particular, strong exchange coupling between the redox-active tpyPY2Me ligand and iron(II) center promotes electrochemical reduction of CO$_2$ to CO at low overpotentials with greater than 90% selectivity and high turnover frequencies. Synthetic reduction of the complex enables access to the catalytically active species [Fe(tpyPY2Me)]^0, which exhibits an unusual open-shell singlet ground state comprised of an intermediate-spin iron(II) (S_{Fe} = 1) antiferromagnetically coupled to a doubly-reduced triplet

terpyridine ligand ($S_{tpy} = 1$). Significantly, this unique electronic structure also enables this catalyst to operate in water with a high selectivity for CO_2 reduction over the hydrogen evolution reaction.

RESULTS AND DISCUSSION

The tpyPY2Me ligand and corresponding iron(II) complex $[Fe(tpyPY2Me)(CH_3CN)]^{2+}$ (**[Fe1]²⁺**) were prepared following modifications of previously reported procedures for PY5Me₂ and its complexes (see supplementary information). In order to understand the role of the iron center in catalysis, we also prepared the diamagnetic zinc(II) analog $[Zn(tpyPY2Me)]^{2+}$ (**[Zn1]²⁺**). Finally, we prepared the complexes $[Fe(PY5Me_2)(CH_3CN)]^{2+[20]}$ and $[Zn(PY5Me_2)(CH_3CN)]^{2+[16]}$ to aid in identifying the role of the redox-active terpyridine fragment of the polypyridyl scaffold. A comparison of the solid-state structures of **[Fe1]²⁺** and $[Fe(PY5Me_2)(CH_3CN)]^{2+[20]}$ obtained via single-crystal X-ray diffraction revealed that the enhanced rigidity of the tpyPY2Me ligand enforces a more distorted *pseudo*-octahedral (O_h) geometry in **[Fe1]²⁺** relative to $[Fe(PY5Me_2)(CH_3CN)]^{2+}$, which adopts an almost ideal O_h geometry (Figure 1b and Figure S1; Tables S1–S4). In particular, occupation of the iron equatorial plane by the three terpyridine nitrogen atoms and coordination of the pyridine arms to axial and equatorial positions induces severe axial distortions in **[Fe1]²⁺** that are absent in $[Fe(PY5Me_2)(CH_3CN)]^{2+}$ (Table S2). This distortion also significantly compresses the axial bond angle in **[Fe1]²⁺** (173.64(6)°) whereas the corresponding angle in $[Fe(PY5Me_2)(CH_3CN)]^{2+}$ is nearly linear (178.53(7)°) (Figure 1C).

The structure of **[Fe1]²⁺** remains more distorted than that of $[Fe(PY5Me_2)(CH_3CN)]^{2+}$ in solution, as verified by ¹H NMR spectra collected for both complexes in CD_3CN at 295 K. The spectrum of $Fe(PY5Me_2)(CH_3CN)]^{2+}$ features five sharp signals consistent with a C_{2v} symmetric complex with low-spin Fe^{2+} ($S = 0$), whereas the ¹H NMR spectrum of **[Fe1]²⁺** features slightly more broadened resonances with no well-defined symmetry (Figure S2). Using the Evans method,
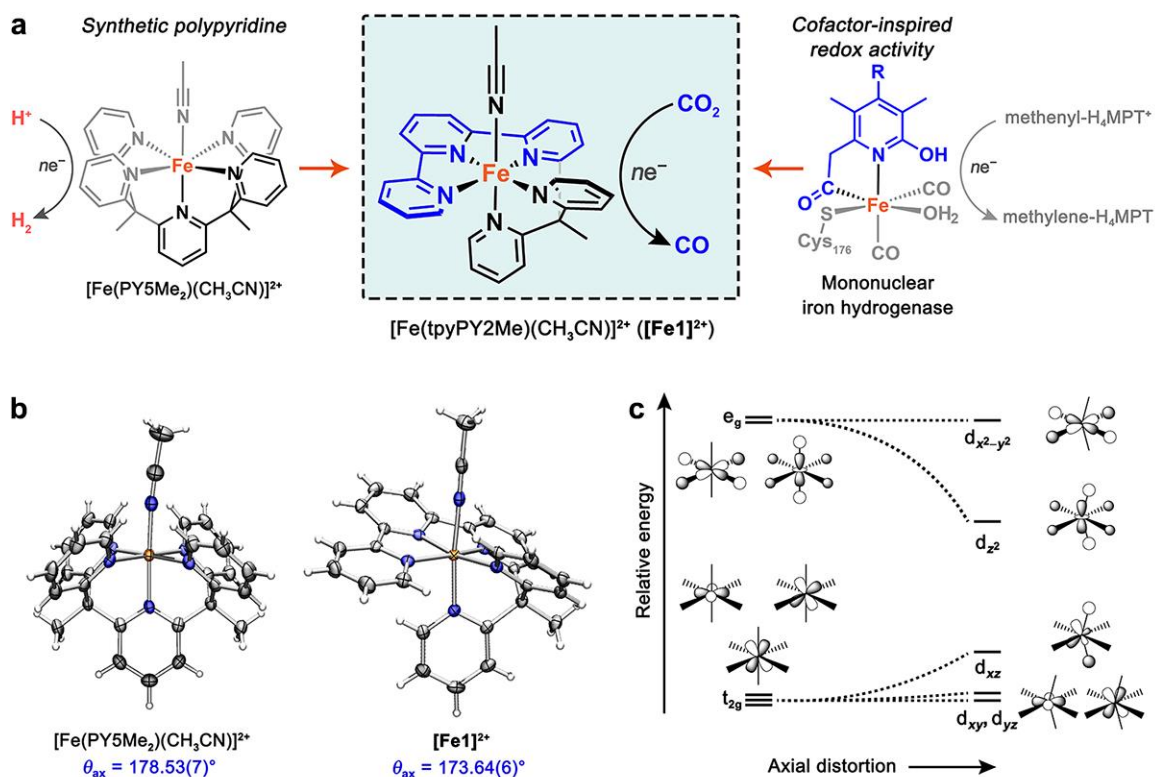
Figure 1. Design and structural characterization of iron polypyridyl complexes. (**A**) The molecular CO_2 reduction catalyst **[Fe1]$^{2+}$** was designed to feature a redox-active pendant in a robust synthetic polypyridyl scaffold, inspired by the active site of mononuclear iron hydrogenase. (**B**) Solid state structures of [Fe(PY5Me$_2$)(CH$_3$CN)]$^{2+}$, featuring redox-innocent PY5Me$_2$ ligand, and **[Fe1]$^{2+}$**, as determined via X-ray diffraction analysis. Thermal ellipsoids are plotted at 80% probability level; orange, blue, and gray ellipsoids represent Fe, N, and C atoms, respectively. Hydrogen atoms, noncoordinating solvent, and anions are omitted for clarity. (**C**) Simplified Walsh diagram illustrating the effect of axial distortion away from the near ideal O_h symmetry in [Fe(PY5Me$_2$)(CH$_3$CN)]$^{2+}$ toward C_{2v} symmetry in **[Fe1]$^{2+}$**.

we measured a room temperature magnetic moment of 1.93 μ_B for **[Fe1]$^{2+}$**, which is indicative of

an intermediate-spin Fe^{2+} ($S = 1$) ground state (Figure S3). Because the **[Fe1]$^{2+}$** bond lengths

measured at 100 K are in agreement with those of other low-spin Fe^{2+} polypyridyl complexes[20],

the collective data suggest that **[Fe1]$^{2+}$** undergoes a spin-state transition between 100 K and room

temperature. In line with this interpretation, at ~300 K the ^{1}H NMR spectrum of **[Fe1]$^{2+}$** displays

severe line broadening consistent with paramagnetic iron(II), whereas cooling to 233 K results in

a spectrum with much shaper peaks, indicative of an increase in the population of low-spin iron(II)

(Figure S4). Zero-field ^{57}Fe Mössbauer spectra collected for **[Fe1]$^{2+}$** at 5 and 295 K further support

such a spin state transition (Figures S5–6 and Tables S5–6). At 5 K, the spectrum features a

symmetric Lorentzian doublet with isomer shift (δ) and quadrupole splitting ($|\Delta E_Q|$) values of 0.3562(4) and 1.0203(8) mm/s, respectively, consistent with a low-spin iron(II) as corroborated by density functional theory (DFT) calculations (Tables S5–6)[21,22]. In contrast, the Mössbauer spectrum measured at 295 K features an asymmetric quadrupole doublet that can be fit to two iron sites. The parameters of the major site (84(1)%) are nearly identical to the 5 K spectrum when accounting for second-order doppler effects ($\delta = 0.285(1)$ mm/s, $|\Delta E_Q| = 1.056(2)$ mm/s), while the isomer shift of the minor site (16(1)%) is 0.62(1) mm/s, indicative of a higher spin-state iron(II) species. The distinct iron(II) spin states in **[Fe1]$^{2+}$** and [Fe(PY5Me$_2$)(CH$_3$CN)]$^{2+}$ can be understood from the simplified Walsh diagram presented in Figure 1c. Axial distortions engendered by the rigid tpyPY2Me ligand lead to a decrease in symmetry from idealized O_h to C_{2v}, and this distortion significantly stabilizes the d$_{z^2}$ orbital and destabilizes the d$_{xz}$ through z-component mixing of the t$_{1u}$ and t$_{2g}$ orbitals. The stabilization of the d$_{z^2}$ orbital and disruption of t$_{2g}$ degeneracy facilitates the formation of intermediate-spin iron(II) in **[Fe1]$^{2+}$** near ambient temperature. These marked differences in the ground-state electronic structures of **[Fe1]$^{2+}$** and Fe(PY5Me$_2$)(CH$_3$CN)]$^{2+}$ contribute to their distinct electrochemical and catalytic behavior (*vide infra*).

The presence of a redox-active terpyridine moiety in tpyPY2Me also gives rise to unique electrochemical behavior for **[Fe1]$^{2+}$** and **[Zn1]$^{2+}$** relative to their PY5Me$_2$ analogues. The room-temperature cyclic voltammogram (CV) of **[Fe1]$^{2+}$** collected in CH$_3$CN under Ar exhibits two reversible features: a one-electron reduction at $E_{1/2} = 0.66$ V (versus Fc/Fc$^+$) assigned to the iron(III/II) couple and a two-electron redox process assigned to tpyPY2Me$^{0/2-}$ at −1.43 V (Figure 2a). No additional features were observed when scanning to more negative potentials. Under the same conditions, the cyclic voltammogram of **[Zn1]$^{2+}$** exhibits two reversible, one-electron ligand-centered reductions at $E_{1/2} = -1.56$ and −2.07 V and an additional irreversible redox event
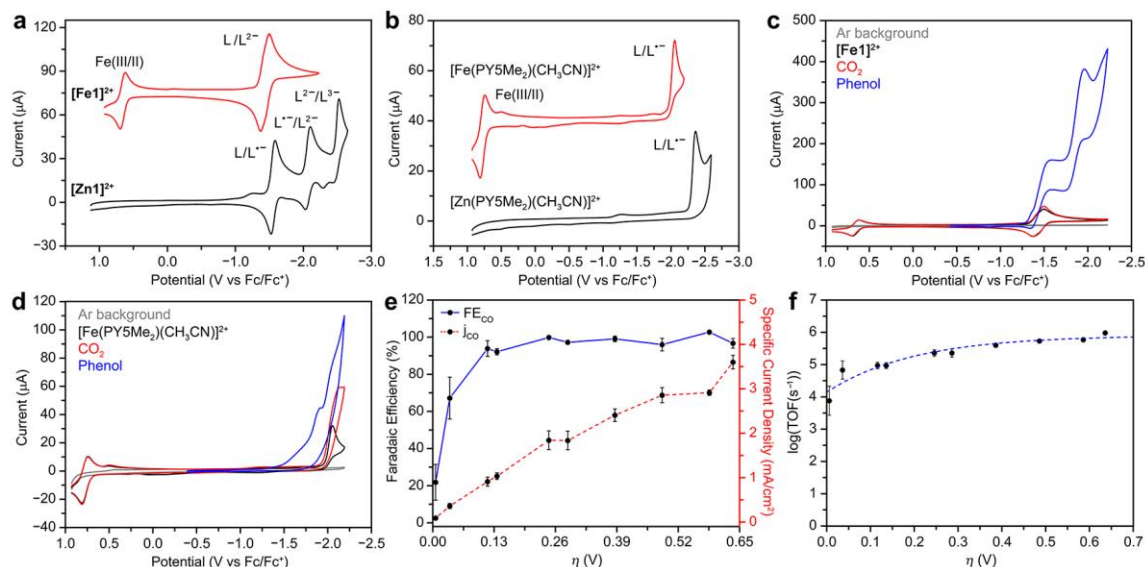
Figure 2. Electrochemical characterization and CO₂ reduction performance. Cyclic voltammograms collected under Ar of (**A**) **[Fe1]²⁺** (red trace) and **[Zn1]²⁺** (black trace) complexes and (**B**) $[Fe(PY5Me_2)(CH_3CN)]^{2+}$ (red trace) and $[Zn(PY5Me_2)(CH_3CN)]^{2+}$ (black trace) complexes supported by redox-innocent PY5Me₂. Cyclic voltammograms of (**C**) **[Fe1]²⁺** and (**D**) $[Fe(PY5Me_2)(CH_3CN)]^{2+}$ collected under Ar (black), CO₂ (red), and with added phenol (3.5 M, blue). (**E**) Selectivity of **[Fe1]²⁺** for CO₂ reduction to CO at varying overpotentials and specific current densities for CO (j_{CO}) production (averages of three experiments). (**F**) Catalytic Tafel plot for **[Fe1]²⁺** obtained from CPE experiments in acetonitrile with added phenol (3.5 M).

(tpyPY2Me$^{2-/3-}$) at −2.41 V (Figure 2a), which indicates a degree of communication between the reduced tpyPY2Me ligand and iron that is not possible in the isostructural zinc complex. In contrast, ligand-based reduction in $[Fe(PY5Me_2)(CH_3CN)]^{2+}$ and $[Zn(PY5Me_2)(CH_3CN)]^{2+}$ is irreversible and occurs at potentials negative of –2.0 V, highlighting the crucial role of the terpyridyl fragment in achieving electrochemically reversible reduction events at relatively positive potentials.

Under an atmosphere of CO₂, CV data collected for **[Fe1]²⁺** exhibit only a subtle increase in current relative to scans under Ar; however, when excess phenol (3.5 M) is added as a proton source, two large catalytic waves appear at *ca.* –1.50 and –2.0 V versus Fc/Fc⁺ (Figure 2c). $[Fe(PY5Me_2)(CH_3CN)]^{2+}$ also displays catalytic currents after addition of CO₂ and phenol, but the onset current for catalysis is >500 mV more negative than that observed for **[Fe1]²⁺** (Figure 2d). Phenol titrations conducted with solutions of **[Fe1]²⁺** under a CO₂ atmosphere revealed a dose-

dependence on phenol concentration (Figure S7). The electrochemical response is mitigated when control phenol titrations are collected under an Ar atmosphere, suggesting that $[\mathbf{Fe1}]^{2+}$ selectively catalyzes electrochemical CO_2 reduction over the hydrogen evolution reaction, even at high concentrations of organic acid (Figure S7). Indeed, preparative-scale controlled potential electrolysis (CPE) experiments were conducted in CO_2-saturated acetonitrile with 3.5 M phenol across a range of overpotentials (η = 0.006–0.636 V), and quantification of products by gas chromatography revealed that CO is the major product under all conditions (Figures S8–S10). The thermodynamic potential for CO_2 reduction to CO was determined in acetonitrile using the pK_a for carbonic acid[23]. $[\mathbf{Fe1}]^{2+}$ is highly selective for CO_2 reduction over hydrogen evolution across the entire potential window examined, with current densities for CO production (j_{CO}) reaching as high as 3.6 mA/cm^2 (Figure 2e and Figure S11). The Faradaic efficiency for CO production (FE$_{CO}$) reaches 94% at an overpotential of 116 mV and increases to nearly 100% with the application of overpotentials between 246 and 636 mV (Figures 2e and S11). Significantly, only small amounts of H$_2$ (FE$_{H_2}$ = 44%) were detected in analogous CPE experiments with $[Fe(PY5Me_2)(CH_3CN)]^{2+}$ at much larger overpotentials (Figure S12). Control experiments strongly support the homogenous molecular nature of the catalysis with $[\mathbf{Fe1}]^{2+}$ and its high selectivity for CO_2 reduction. First, CO_2 reduction was not observed in the absence of $[\mathbf{Fe1}]^{2+}$ (Figure S13). Furthermore, cyclic voltammetry and UV-vis data collected before and after 1-hour CPE experiments are indistinguishable, attesting to the bulk stability of $[\mathbf{Fe1}]^{2+}$ under electrolysis conditions (Figure S14). Finally, the possible formation of an electrode-adsorbed active catalyst was excluded through a series of control experiments. Peak currents for $[\mathbf{Fe1}]^{2+}$ and $[\mathbf{Zn1}]^{2+}$ scale linearly with the square root of the scan rate, indicative of freely diffusing species in solution (Figures S15–16). In addition, CPE rinse tests, which probe for electrode deposition, give complete inversion of

product selectivity, with H_2 as the predominant product and negligible generation of CO (Figure S17).

Encouraged by the high selectivity of **[Fe1]$^{2+}$** for CO_2 reduction over the hydrogen evolution reaction, we sought to evaluate its kinetic performance. Cyclic voltammograms acquired for **[Fe1]$^{2+}$** under CO_2-saturated electrolyte in the presence of 3.5 M phenol (Figure S18) exhibit scan rate dependence and noncanonical peak-shaped waves, indicative of competitive, nonideal processes (*e.g.,* substrate consumption, catalyst deactivation, etc.). As a result, k_{obs} (TOF$_{max}$) obtained from catalytic plateau current analysis underestimates rates of CO_2 reduction[24]. We instead determined kinetic parameters directly from our variable-potential CPE experiments with direct product detection (Figure 2f)[25] and in parallel applied foot-of-the-wave analysis as pioneered by Savéant[25] to extract kinetic information from our CV data (Figure S19). The latter analysis estimates the idealized catalytic reactivity by considering the initial portion of the catalytic wave where the effects of side phenomena are expected to be minimal. Reasonable agreement between the two methods was found, and a TOF of 100,000 s^{-1} was measured at an applied overpotential of 116 mV by direct CPE product analysis. Slight discrepancies between the two methods are attributed to the limited linear foot-of-the-wave region (Figure S19). Nevertheless, catalytic Tafel plots constructed from either the variable-potential CPE data (Figure 2f) or foot-of-the-wave analysis (Figure S19) identify **[Fe1]$^{2+}$** as one of the most active molecular electrocatalysts reported to date, achieving TOFs >500,000 s^{-1} at overpotentials below 500 mV (Figure S20). Notably, this rapid, homogeneous CO_2 reduction catalysis is achieved without any modifications to the secondary coordination sphere to introduce hydrogen bond/proton-relay functionalities to break electronic scaling relationships[23,26–31]. Finally, to assess the catalytic stability of **[Fe1]$^{2+}$**, four consecutive five-hour CPE experiments were conducted at −1.98 V (versus Fc/Fc$^+$), the highest

potential investigated, without addition of fresh **[Fe1]$^{2+}$** between each experiment (Figure S21).
[Fe1]$^{2+}$ is remarkably stable with over 200 C of charge passed over the 20-hour window without
any loss in selectivity for CO (average FE$_{CO}$ = 87%).
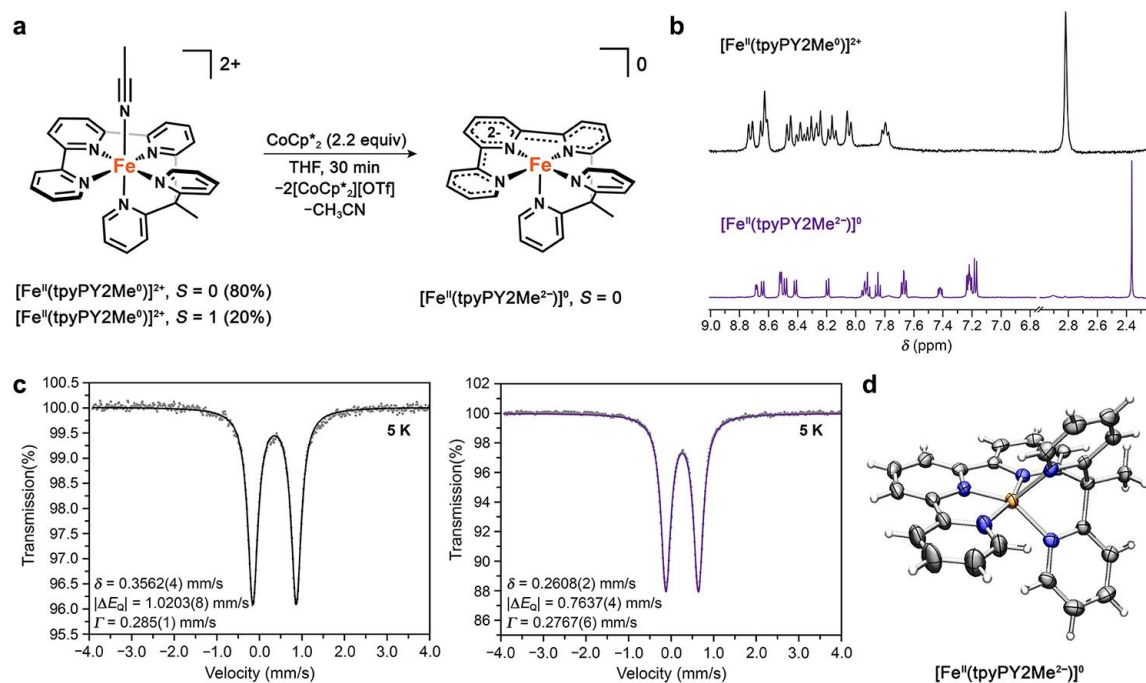
Figure 3. Preparation and characterization of open-shell singlet species [Fe1]^0. (**A**) Two-electron reduction
of **[Fe1]$^{2+}$** generates the catalytically active **[Fe1]^0** complex. (**B**) ^{1}H NMR spectrum of **[Fe1]$^{2+}$** (black) and ^{1}H
NMR spectrum of the product resulting from chemical reduction of **[Fe1]$^{2+}$** with CoCp*$_2$ (purple); both spectra
were in CD$_3$CN at room temperature. (**C**) Zero-field ^{57}Fe Mössbauer analysis of **[Fe1]$^{2+}$** (black) and **[Fe1]^0**
(purple) measured at 5 K. (**D**) Solid state structure of **[Fe1]^0** from single-crystal X-ray diffraction analysis.
Thermal ellipsoids are plotted at 80% probability level; orange, blue, and grey ellipsoids represent Fe, N, and C
atoms, respectively. Residual solvent, and co-crystalized CoCp*$_2$ are omitted for clarity.

We reasoned that the observed electrocatalytic efficiency for **[Fe1]$^{2+}$** for CO$_2$ reduction stems
from a synergistic effect between the iron center and the redox-active tpyPY2Me ligand. To
establish a molecular-level understanding of such cooperativity, we sought to isolate and
characterize the catalytically relevant, two-electron reduced complex [Fe(tpyPY2Me)]^0 (**[Fe1]^0**).
Chemical reduction of **[Fe1]$^{2+}$** with 2.2 equivalents of decamethylcobaltocene (Figure 3a)
produced **[Fe1]^0** as a dark purple solid. Interestingly, room temperature ^{1}H NMR analysis of **[Fe1]^0**
in CD$_3$CN revealed that the compound is diamagnetic with the aryl and aliphatic signals shifted

upfield (Figure 3b). A nearly identical NMR spectrum was obtained for the product **[Zn1]⁰** generated from the chemical reduction of **[Zn1]²⁺** with potassium graphite (see Figure S22 and details in the supplementary materials). These data are consistent with our assignment of the reduction features for both **[Fe1]²⁺** and **[Zn]²⁺** as ligand-centered events. Given the unique diamagnetic ground state of **[Fe1]⁰**, two electronic structures are possible. The first possibility is a low-spin iron(II) center ($S_{Fe} = 0$) coordinated to a reduced closed-shell singlet ligand ($S_{tpy} = 0$) generated by both electrons occupying the same π^* orbital. The other possibility is an intermediate-spin iron(II) center ($S_{Fe} = 1$) antiferromagnetically coupled to a reduced ligand with an open-shell triplet configuration ($S_{tpy} = 1$) through half occupation of both low-lying π^* terpyridine orbitals, leading to an overall open-shell singlet electronic structure. The large anodic shift (> 600 mV) in the ligand-based reductions of **[Fe1]²⁺** relative to **[Zn1]²⁺** strongly supports the latter electronic configuration. Mössbauer data for **[Fe1]²⁺** and **[Fe1]⁰** further revealed that reduction causes a significant decrease in the isomer shift and quadrupole splitting (from $\delta = 0.3562(4)$ mm/s and $|\Delta E_Q| = 1.0203(8)$ mm/s to $\delta = 0.2608(2)$ mm/s and $|\Delta E_Q| = 0.7637(4)$ mm/s, respectively), consistent with the formation of intermediate-spin iron(II) (Figure 3c)[32]. Mössbauer parameters predicted from DFT also support this assignment (Table S6)[21,22]. The antiferromagnetic coupling between the reduced biradical ligand (tpyPY2Me²⁻) and intermediate-spin Fe²⁺ is expected to be quite strong, given that identical Mössbauer spectra are obtained for **[Fe1]⁰** at 295 and 5 K (after accounting for second-order Doppler effects) (Figure S23) and a diamagnetic ¹H NMR spectrum is observed at room temperature. Indeed, DFT calculations predict a large coupling constant of −1023 cm⁻¹, giving rise to a singlet-quintet gap of 4400 cm⁻¹ (see the supplementary materials).

The solid-state structure of **[Fe1]⁰** also supports the presence of an open-shell singlet electronic structure promoted through strong metal–ligand exchange coupling. Single crystals of **[Fe1]⁰** were

obtained by slow evaporation of a saturated acetonitrile solution, and X-ray diffraction analysis revealed a distorted square pyramidal geometry (Figure 3d) resulting from the loss of the axial acetonitrile ligand in $[\textbf{Fe1}]^{2+}$. The terpyridine bond metrics enable us to directly distinguish between the two possible electronic configurations of $[\textbf{Fe1}]^{0}$, as a result of the unique bonding interactions of the terpyridine LUMOs[33]. The experimental bond lengths agree most closely with those from the optimized structure of the antiferromagnetically coupled open-shell singlet (Figure 3d; Table S9). Furthermore, a comparison of the terpyridine bond lengths to those reported for reduced, homoleptic bis(terpyridine) complexes ($[M(tpy)_2]^{n+}$; M = Cr, Fe)[34,35] strongly suggests that both π^* orbitals in $[\textbf{Fe1}]^{0}$ are half-occupied (Table S10). Taken together, the electrochemical, NMR, Mössbauer, and X-ray diffraction data establish that the catalytically relevant $[\textbf{Fe1}]^{0}$ species possesses a unique, open-shell singlet ground state composed of an intermediate-spin iron(II) center ($S_{Fe} = 1$) that is antiferromagnetically coupled to a doubly-reduced tpyPY2Me ($S_{tpy} = 1$). This strong exchange coupling shifts the tpyPY2Me-based reductions of $[\textbf{Fe1}]^{2+}$ to more positive potentials and ultimately promotes selective and efficient CO_2 reduction catalysis.

We carried out DFT calculations using the ωB97X-D functional to generate a more accurate molecular orbital picture of our $[\textbf{Fe1}]^{2+}$ system. Optimized structures and predicted redox potentials for $[\textbf{Fe1}]^{2+}$ and $[\textbf{Zn1}]^{2+}$ are in good agreement with experimental data (Tables S11–12). Interestingly, although the DFT data indicate the metal center in $[\textbf{Fe1}]^{2+}$ is best described as low-spin iron(II), the calculated singlet-quintet gap is small, explaining the observed thermal population of a higher spin-state at room temperature (Tables S13–14). The first reduction of $[\textbf{Fe1}]^{2+}$ to $[\textbf{Fe1}]^{+}$ is predicted to generate a ground state doublet composed of a low-spin iron(II) and a tpyPY2Me-based radical with a predicted redox potential of −1.46 V (Figure 4a–c). The spin density plot of this $[\textbf{Fe1}]^{+}$ species indicates ligand-based reduction with almost no excess spin on
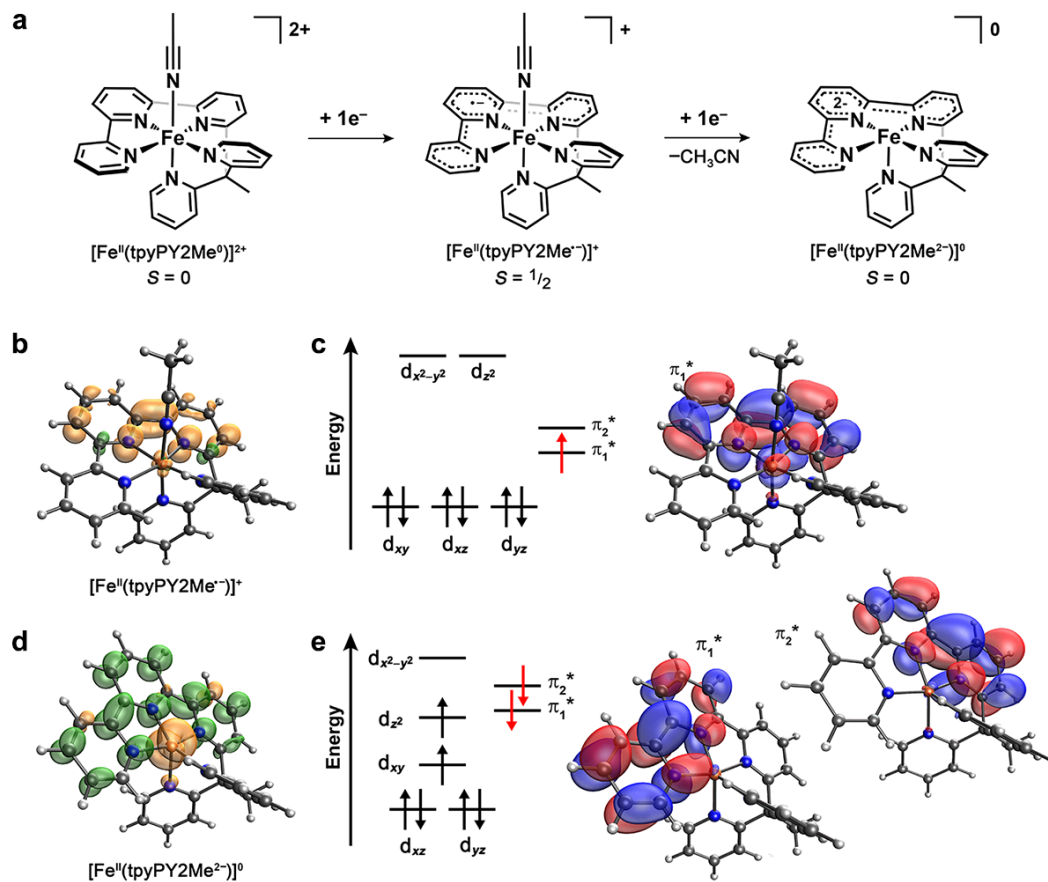
Figure 4. DFT analysis and calculated molecular orbitals for [Fe1]$^+$ and [Fe1]^0 species. (**A**) DFT predicted pathway for reduction of **[Fe1]$^{2+}$** to **[Fe1]^0**. (**B**) Spin density plot and (**C**) simplified molecular orbital diagram of the one electron reduced intermediate **[Fe1]$^+$**. (**D**) Spin density plot and (**E**) simplified molecular orbital diagram of **[Fe1]^0**. Localized metal orbitals are depicted in the supplementary materials.

the iron center (Figure 4b). The second reduction populates a second low lying π^* orbital of tpyPY2Me and induces loss of the axial acetonitrile molecule, providing access to an intermediate-spin iron(II) state (Figure 4a,d,e). The $S_{Fe} = 1$ iron center is strongly antiferromagnetically coupled to the two electrons in the tpyPY2Me π^* orbitals (Figure 4e). Localized orbital bonding analysis confirmed that iron remains in the 2+ oxidation state during the second reduction process, which has a predicted reduction potential of -1.51 V. This broken symmetry solution is significantly lower in energy (12 kcal/mol) than the other feasible singlet consisting of low-spin iron(II) ($S_{Fe} = 0$) and doubly reduced ligand ($S_{tpy} = 0$) (Tables S13–14). To further probe the entanglement of the

two ligand-based orbitals and two metal d-orbitals, we employed multiconfigurational wave-function methods (see the supplementary information), which confirmed the antiferromagnetically coupled ground state. In particular, the axial distortion away from octahedral symmetry allows the d_{z^2} and d_{xy} metal orbitals to interact with the two tpyPY2Me π^* orbitals in a weak π-type interaction (Figure S24). Interestingly, the calculated potential difference for the second reduction event in **[Zn1]$^{2+}$** and **[Fe1]$^{2+}$** is approximately 0.5 V. This shift agrees with the energy difference between the two **[Fe1]^{0}** singlet states, further indicating that significant stabilization is achieved through this unique open-shell singlet conformation.
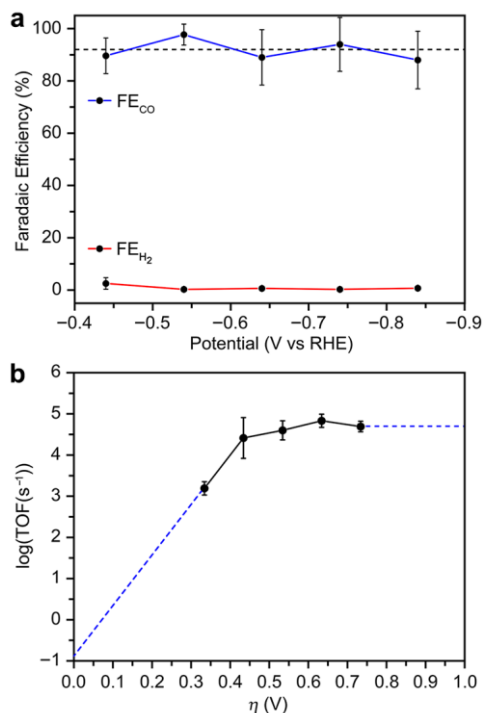
Figure 5. Aqueous CO$_2$ reduction performance. (**A**) Faradaic efficiencies for CO (blue) and H$_2$ (red) formation at varying applied potentials for 60 min (averages of three experiments). The average FE$_{CO}$ is indicated by the black dashed line. (**B**) Catalytic Tafel plot for **[Fe1]$^{2+}$** obtained from CPE experiments in 0.10 M NaHCO$_3$. The dashed blue line shows data extrapolation with an approximate TOF$_{max}$ of 50,000 s^{-1}.

Given the low overpotentials required for **[Fe1]$^{2+}$** to catalyze homogeneous electrochemical CO$_2$ reduction in organic solvent, we sought to evaluate its activity in water (Figure 5). For this

purpose, we prepared the more water-soluble nitrate analog of **[Fe1]$^{2+}$** (see the supplementary materials), and X-ray diffraction analysis revealed that anion exchange does not alter the catalyst structure (Figure S25; Tables S15–16). As a cheap, abundant, and benign solvent and proton source, water is an attractive medium for CO_2 reduction. However, molecular CO_2 reduction catalysts typically require precious metals or mercury working electrodes to operate effectively in aqueous electrolytes, because their onset potentials are too negative to be compatible with more desirable carbon-based electrodes that preferentially catalyze competing water reduction[36–40]. Cyclic voltammograms collected for **[Fe1]$^{2+}$** in 0.10 M $NaHCO_3$ with a carbon paste working electrode show the formation of a catalytic wave when saturated with CO_2 (Figure S26). Notably, variable potential CPE experiments revealed that **[Fe1]$^{2+}$** maintains its activity and selectivity for CO_2 reduction to CO in water (average $FE_{CO} = 92\%$ and $FE_{H_2} < 1\%$) with maximum turnover frequencies reaching >50,000 s^{-1} at overpotentials of 500 mV (Figure 5). Importantly, control rinse tests passed negligible current during one-hour CPE experiments, and the selectivity was inverted such that H_2 is the major product (Figures S27–32). Electrochemical stripping behavior is also observed, which may contribute to slower catalysis in water relative to organic solvent (Figure S33). Nevertheless, these data show that **[Fe1]$^{2+}$** is an effective molecular catalyst for homogeneous CO_2 reduction in water. Crucially, given its molecular nature, the activity, stability, and overpotential of this catalyst can in principle be tuned through ligand modifications accessible by synthetic chemistry. Further, the study of this catalyst and related systems has the potential to shed important insights on the behavior of materials catalysts bearing atomically dispersed iron sites[41].

CONCLUDING REMARKS

The ability to create molecular compounds with strong exchange coupling between synergistic, redox non-innocent ligands and metal centers has broad implications for catalyst design, including enabling control over the density and arrangement of functional active sites. Indeed, redox balancing through electronic delocalization is pivotal for biological and materials catalysts to achieve complex chemical transformations at or near thermodynamic potentials. However, discrete molecular compounds offer a level of tunability via coordination chemistry that remains unparalleled in protein design and nanostructure engineering. Thus, inorganic molecules are uniquely positioned to open up access to a range of new properties and offer a desirable alternative strategy for lowering energy barriers for redox catalysis.

ASSOCIATED CONTENT

Supporting Information. Experimental and computational details, compound characterization, supplemental electrochemical and spectroscopic data, and DFT geometry optimized atomic xyz coordinates is available free of charge.

AUTHOR INFORMATION

Corresponding Author

*Christopher J. Chang – Departments of Chemistry and Molecular and Cell Biology University of California, Berkeley, CA, 94720, USA; Chemical Sciences Division, Lawrence Berkeley National Laboratory, Berkeley, CA, 94720, USA. ocid.org/0000-0001-5732-9497; Email: chrischang@berkeley.edu

Authors

Jeffrey S. Derrick – Department of Chemistry University of California, Berkeley, CA, 94720, USA; Chemical Sciences Division, Lawrence Berkeley National Laboratory, Berkeley, CA, 94720, USA. orcid.org/0000-0002-3879-2897.

Matthias Loipersberger – Department of Chemistry University of California, Berkeley, CA, 94720, USA.

Diana A. Iovan – Department of Chemistry University of California, Berkeley, CA, 94720, USA. orcid.org/0000-0001-9889-7183.

Peter T. Smith – Department of Chemistry University of California, Berkeley, CA, 94720, USA; Chemical Sciences Division, Lawrence Berkeley National Laboratory, Berkeley, CA, 94720, USA. orcid.org/0000-0002-8892-3752.

Khetpakorn Chakarawet – Department of Chemistry University of California, Berkeley, CA, 94720, USA. orcid.org/0000-0001-5905-3578.

Jeffrey R. Long – Departments of Chemistry and Chemical and Biochemical Engineering University of California, Berkeley, CA, 94720, USA; Materials Sciences Division, Lawrence Berkeley National Laboratory, Berkeley, CA, 94720, USA. orcid.org/0000-0002-5324-1321.

Martin Head-Gordon – Department of Chemistry University of California, Berkeley, CA, 94720, USA; Chemical Sciences Division, Lawrence Berkeley National Laboratory, Berkeley, CA, 94720, USA. orcid.org/0000-0002-4309-6669

REFERENCES

(1) Lewis, N. S.; Nocera, D. G. Powering the planet: chemical challenges in solar energy utilization. *Proc. Natl. Acad. Sci. USA*, **2006**, *103*, 15729–15735.

(2) Luna, P. D.; Hahn, C; Higgins, D.; Jaffer, S. A.; Jaramillo, T. F.; Sargent, E. H. What would it take for renewably powered electrosynthesis to displace petrochemical processes? *Science*, **2019**, *364*, doi:10.1126/science.aav3506.

(3) Francke, R.; Schille, B; Roemelt, M. Homogenously catalyzed electroreduction of carbon dioxide–methods, mechanisms, and catalysts. *Chem. Rev.* **2018**, *118*, 4631–4701.

(4) Can, M.; Armstrong, F. A.; Ragsdale, S. W. Structure, function, and mechanism of the nickel metalloenzymes, CO dehydrogenase, and acetyl-CoA synthase. *Chem. Rev.* **2014**, *114*, 4149–4174.

(5) Corbin, N.; Zeng, J.; Williams, K.; Manthiram, K. Heterogenous molecular catalysts for electrochemical CO_2 reduction. *Nano Res.* **2019**, *12*, 2093–2125.

(6) Fisher, B. J.; Eisenberg, R. Electrocatalytic reduction of carbon dioxide by using macrocycles of nickel and cobalt. *J. Am. Chem. Soc.* **1980**, *102*, 7361–7363.

(7) Beley, M.; Collin, J.-P.; Ruppert, R.; Sauvage, J.-P. Nickel(II)-cyclam: an extremely selective electrocatalyst for reduction of CO_2 in water *J. Chem. Soc., Chem. Commun.*, **1984**, 1315–1316.

(8) Hammouche, M.; Lexa, D.; Savéant, J. M.; Momenteau, M. Catalysis of the electrochemical reduction of carbon dioxide by iron("0") porphyrins. *J. Electroanal. Chem.* **1988**, *249*, 347–351.

(9) Meshitsuka, S.; Ichikawa, M.; Tamaru, K. Electrocatalysis by metal phthalocyanines in the reduction of carbon dioxide. *J. Chem. Soc., Chem. Commun.*, **1974**, 158–159 (1974).

(10) Ren, S.; Joulié, D.; Salvatore, D.; Torbensen, K.; Wang, M.; Berlinguette, C. P. Molecular electrocatalysts can mediate fast, selective CO_2 reduction in a flow cell. *Science*. **2019**, *365*, 367–369.

(11) Hawecker, J.; Lehn, J.-M.; Ziessel, R. Electrocatalytic reduction of carbon dioxide mediated by $Re(bipy)(CO)_3Cl$ (bipy = 2,2'-bipyridine). *J. Chem. Soc., Chem. Commun.*, **1984**, 328–330.

(12) Smieja, J. M.; Kubiak, C. P. $Re(bipy-tBu)(CO)_3Cl$-improved catalytic activity for reduction of carbon dioxide: IR-spectroelectrochemical and mechanistic studies. *Inorg. Chem.* **2010**, *49*, 9283–9289.

(13) Karunadasa, H. I.; Chang, C. J.; Long, J. R. A molecular molybdenum-oxo catalyst for generating hydrogen from water. *Nature* **2010** *464*, 1329–1333.

(14) Karunadasa, H. I.; Montalvo, E.; Sun, Y.; Majda, M.; Long, J. R.; Chang, C. J. A molecular MoS_2 edge site mimic for catalytic hydrogen generation. *Science* **2012**, *335*, 698–702.

(15) Zee, D. Z.; Chantarojsiri, T.; Long, J. R.; Chang, C. J. Metal–polypyridyl catalysts for electro- and photochemical reduction of water to hydrogen. *Acc. Chem. Res.* **2015** *48*, 2027–2036.

(16) Sun, Y.; Bigi, J. P.; Piro, N. A.; Tang, M. L.; Long, J. R.; Chang, C. J. Molecular cobalt pentapyridine catalysts for generating hydrogen from water. *J. Am. Chem. Soc.* **2011**, *133*, 9212–9215.

(17) Wu, Y.; Jiang, J.; Weng, Z.; Wang, M.; Broere, D. L. J.; Zhong, Y.; Brudvig, G. W.; Feng, Z.; Wang, H. Electroreduction of CO_2 catalyzed by a heterogenized Zn-porphyrin complex with a redox-innocent metal center. *ACS Cent. Sci.* **2017**, *3*, 847–852.

(18) Su, X.; McCardle, K. M.; Panetier, J. A.; Jurss, J. W. Electrocatalytic CO_2 reduction with nickel complexes supported by tunable bipyridyl-N-heterocyclic carbene donors: understanding redox-active macrocycles. *Chem. Commun.* **2018**, *54*, 3351–3354.

(19) Dey, S.; Das, P. K.; Dey, A. Mononuclear iron hydrogenase. *Coord. Chem. Rev.* **2013,** *257*, 42–63.

(20) Chantarojsiri, T.; Sun, Y.; Long, J. R.; Chang, C. J. Water-soluble iron(IV)-oxo complexes supported by pentapyridine ligands: axial ligand effects on hydrogen atom and oxygen atom transfer reactivity. *Inorg. Chem.* **2015**, *54*, 5879–5887.

(21) Römelt, M.; Ye, S.; Neese, F. Calibration of modern density functional theory methods for the prediction of [57]Fe Mössbauer isomer shifts: meta-GGA and double-hybrid functionals. *Inorg. Chem.* **2009**, *48*, 784–785.

(22) McWilliams, S. F.; Brennan-Wydra, E.; MacLeod, K. C.; Holland, P. L. Density functional calculations for prediction of [57]Fe Mössbauer isomer shifts and quadrupole splittings in b-diketiminate complexes. *ACS Omega* **2017**, *2*, 2594–2606.

(23) Costentin, C.; Drouet, S.; Robert, M.; Savéant J.-M. A local proton source enhances CO_2 electroreduction to CO by a molecular Fe catalyst *Science* **2012**, *338*, 90–94.

(24) Rountree, E. S.; McCarthy, B. D.; Eisenhart, T. T.; Dempsey, J. L. Evaluation of homogenous electrocatalysts by cyclic voltammetry. *Inorg. Chem.* **2014**, *53*, 9983–10002.

(25) Costentin, C.; Drouet, S.; Robert, M.; Savéant J.-M. Turnover numbers, turnover frequencies, and overpotential in molecular catalysis of electrochemical reactions. Cyclic voltammetry and preparative-scale electrolysis. *J. Am. Chem. Soc.* **2012**, *134*, 11235–11242.

(26) Galan, B. R.; Schöffel, J.; Linehan, J. C.; Seu, C.; Appel, A. M.; Roberts, J. A. S.; Helm, M. L.; Kilgore, U. J.; Yang, J. Y.; DuBois, D. L.; Kubiak, C. J. Electrocatalytic oxidation of formate by $[Ni(P^R_2N^{R'}_2)_2(CH_3CN)]^{2+}$ complexes. *J. Am. Chem. Soc.* **2011**, *133*, 12767–12779.

(27) Azcarate, I.; Costentin, C.; Savéant J.-M. Through-space charge interaction substituent effects in molecular catalysis leading to the design of the most efficient catalyst of CO_2-to-CO electrochemical conversion. *J. Am. Chem. Soc.* **2016**, *138*, 16639–16644.

(28) Sung, S.; Kumar, D.; Gil-Sepulcre, M.; Nippe, M. Electrocatalytic CO_2 reduction by imidazolium-functionalized molecular catalysts. *J. Am. Chem. Soc.* **2017**, *139*, 13993–13996.

(29) Nichols, E. M.; Derrick, J. S.; Nistanaki, S. K.; Smith, P. T.; Chang, C. J. Positional effects of second-sphere amide pendants on electrochemical CO_2 reduction catalyzed by iron porphyrins. *Chem. Sci.* **2018**, *9*, 2952–2960.

(30) Haviv, E.; Azaiza-Dabbah, D.; Carmieli, R.; Avram, L.; Martin, J. M. L.; Neumann, R. A thiourea tether in the second coordination sphere as a binding site for CO_2 and a proton donor promotes the electrochemical reduction of CO_2 to CO catalyzed by a rhenium bipyridine-type complex. *J. Am. Chem. Soc.* **2018**, *140*, 12451–12456.

(31) Chapovetsky, A.; Welborn, M.; Luna, J. M.; Haiges, R.; Miller, T. F. III; Marinescu, S. C. Pendant hydrogen-bond donors in cobalt catalysts independently enhance CO_2 reduction. *ACS Cent. Sci.* **2018**, *4*, 397–404.

(32) Gütlich, P.; Eckhard, B.; Trautwein, A. X. *Mössbauer Spectroscopy and Transition Metal Chemistry Fundamentals and Applications* (Springer, 568).

(33) Garino, C.; Gobetto, R.; Nervi, C.; Salassa, L.; Rosenberg, E.; Ross, J. B. A.; Chu, X.; Hardcastle, K. I.; Sabatini, C. Spectroscopic and computational studies of a Ru(II) terpyridine complex: the importance of weak intermolecular forces to photophysical properties. *Inorg. Chem.* **2007**, *46*, 8752–8762.

(34) Scarborough, C. C.; Lancaster, K. L.; DeBeer, S.; Weyhermüller, T.; Sproules, S.; Wieghardt, K. Experimental fingerprints for redox-active terpyridine in $[Cr(tpy)_2](PF_6)_n$ (n = 3–0), and the remarkable electronic structure of $[Cr(tpy)_2]^{1-}$. *Inorg. Chem.* **2012**, *51*, 3718–3732.

(35) England, J.; Scarborough, C. C.; Weyhermüller, T.; Sproules S.; Wieghardt, K. Electronic structures of the electron transfer series $[M(bpy)_3]^n$, $[M(tpy)_2]^n$, and $[Fe(^tbpy)_3]^n$ (M = Fe, Ru; n = 3+, 2+, 1+, 0, 1-): a Mössbauer spectroscopic and DFT study. *Eur. J. Inorg. Chem.* **2012**, 4605–4621.

(36) Froehlich, J. D.; Kubiak, C. C. Homogenous CO_2 reduction by Ni(cyclam) at a glassy carbon electrode. *Inorg. Chem.* **2012**, *51*, 3932–3934.

(37.) Kang, P.; Meyer, T. J.; Brookhart, M. Selective electrocatalytic reduction of carbon dioxide to formate by a water-soluble iridium pincer catalyst. *Chem. Sci.* **2013**, *4*, 3497.

(38) Costentin, C., Robert, M., Savéant, J.-M. & Tatin, A. Efficient and selective molecular catalyst for the CO_2-to-CO electrochemical conversion in water. *Proc Natl Acad Sci USA*. **2015**, *112*, 6882–6886.

(39) Taheri, A.; Thompson, E. J.; Fettinger, J. C.; Berben, L. A. An iron electrocatalyst for selective CO2 to formate in water: including thermochemical insights. *ACS Catal.* **2015**, *5*, 7140–7151.

(40) Nakada, A.; Ishitani, O Selective electrocatalysis of a water-soluble rhenium(I) complex for CO_2 reduction using water as an electron donor. *ACS Catal.* **2018**, *8*, 354–363.

(41) Gu, J.; Hsu, C.-S.; Bai, L.; Chen, H. M.; Hu, X. Atomically dispersed Fe^{3+} sites catalyze efficient CO_2 electroreduction to CO, *Science*. **2019**, *364*, 1091–1094.

TOC Graphic: